Chapter 4

Strong Coupling for Trapping and Sensing: The Atom-Cavity Microscope

In the work of Ref. [25, 26], much of which is also presented in [19], the sensing and trapping aspects of strong coupling are exploited to realize atom-photon binding within an optical cavity. A deep ($\sim$ 2.5 mK) potential associated with the single-quantum interaction arises from the use of a short cavity with very small mode volume ($l = 10.9\,\mu$m, $w_0 = 14.1\,\mu$m). This cavity, with finesse $F = 480,000$ and $(g, \kappa, \gamma)/2\pi = (110, 14.2, 2.6)$ MHz, gives critical photon and atom numbers $m_0 = 2.7 \cdot 10^{-4}, N_0 = 6.1 \cdot 10^{-3}$. The coherent interaction energy exceeds other relevant energies in the problem, in particular the atomic kinetic energy $E_k \approx k_B \cdot 0.46\,mK$ acquired in the 3-mm fall from the MOT to the cavity mode. Thus an atom can be caught within the cavity if the system can be driven from its ground state to the trapping state when the atom is at a maximum of the cavity field [21, 22, 23, 24].

4.1 Summary of Experimental Results

The implementation of this triggering strategy is summarized in Figure 4.1. Atoms are dropped through the cavity mode while cavity transmission is monitored with a weak probe beam. We define detunings of cavity and probe beam relative to the atomic resonance frequency, i.e., $\Delta_{ca} = \omega_c - \omega_a$ and $\Delta_{pa} = \omega_p - \omega_a$. The cavity is tuned

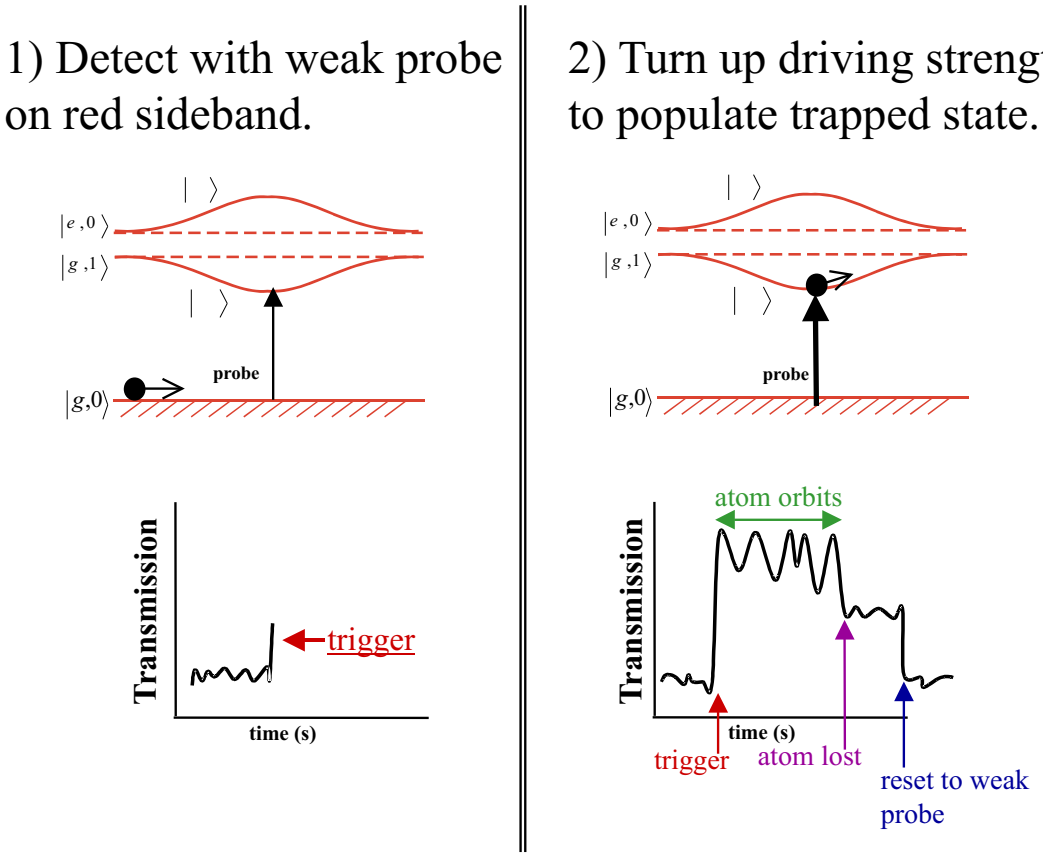

Figure 4.1: Schematic triggered-trapping protocol for the atom-cavity microscope.

slightly below the atomic resonance and the probe is placed near the lower vacuum Rabi sideband of the system, $\Delta_{pa} < \Delta_{ca} < 0$, with a strength of 0.05 intracavity photons. Such a weak probe allows high signal-to-noise for observation of an atom entering the cavity mode, but does not significantly populate the excited states of the atom-cavity system. Once the probe transmission rises above a predetermined threshold, indicating that an atom is in a region of strong coupling to the cavity mode, the probe power is increased to a level of about 0.3 intracavity photons to create a confining potential around the atom.

Figure 4.2(a) shows the resulting cavity transmission for an atom trapped in this way, with parameters $\Delta_{ca}/2\pi = -47$ MHz, $\Delta_{pa}/2\pi = -125$ MHz, and 0.3 photons in the empty cavity. Note that while the "high" probe level is set at 0.3 intracavity photons, the level rises to $|\langle\hat{a}\rangle|^2 \sim 1$ (where $\hat{a}$ is the cavity field annihilation operator) during parts of the measurement record due to the atom's motion within the cavity

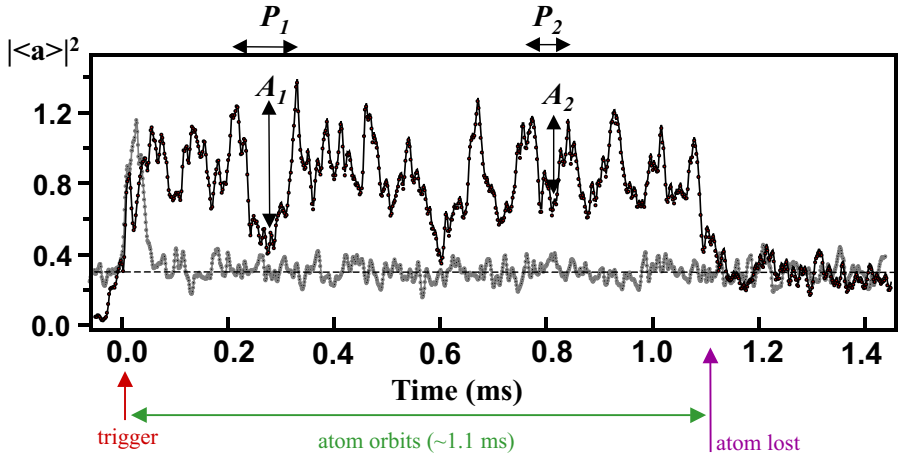

Figure 4.2: Cavity transmission record for a trapped atom moving within the cavity mode. $(\Delta_{pa}, \Delta_{ca})/2\pi = (-125, -47)$ MHz. The probe beam is initially set to 0.05 photons in the empty cavity, and is turned up by a factor of six when triggering occurs. For contrast, an atom freely falling through a constant-strength probe field (0.3 empty-cavity photons) gives the transmission trace shown in gray.

field. Oscillations in transmission arise from atomic motion toward and away from the cavity axis, with the level falling back to 0.3 photons when the atom eventually heats out of the trap and escapes from the cavity. Using this protocol mean atom dwell times in the cavity of 340 μs are observed, with some rare events lasting up to several milliseconds, as compared with the $\sim$ 75 μs free-fall time for an atom to traverse the cavity mode. Lifetimes for a range of different experimental parameters are presented in [19].

Lifetimes are limited by heating associated with the many decays and re-excitations the atom-cavity system experiences during atomic motional timescales. For the parameters of Figure 4.2, the effective potential corresponds to a harmonic oscillation period of $\tau_r = 107$ μs ($\nu_r = 9.38$ kHz) in the radial direction and $\tau_a = 1.46$ μs ($\nu_a = 0.688$ MHz) in the axial direction, while decay and re-excitation are occurring at roughly κ. It is important to note that, while atoms are trapped via their dipole interaction with a red-detuned light field in a manner reminiscent of the more familiar free-space situation, the dynamics associated with the atom-cavity system are quantitatively and qualitatively different from that case [26]. In particular, a free-space potential of equal intensity would exhibit much greater diffusive heating

and thus would largely fail to trap the atoms seen in this experiment (see Section 4.4.2); furthermore, the single-atom sensing which enables the trapping strategy is only available through the use of the cavity QED system.

The most interesting feature of the measurement record for a trapped atom is undoubtedly the oscillation in transmission. The period and amplitude of these oscillations agrees quantitatively with atomic orbital motion in the Gaussian mode transverse to the cavity axis [25, 26]. Referring to Figure 4.2, we see that transmission oscillations exhibit considerable variation in period and amplitude. The examples (A_1, P_1) and (A_2, P_2) suggest that large-amplitude transmission oscillations have longer periods than small-amplitude oscillations. We expect this relationship given the anharmonic (roughly Gaussian) radial potential and initial atomic kinetic energies large enough to substantially sample the anharmonicity. Period P vs. amplitude A are plotted in Figure 4.3 for experimental and simulated transmission oscillations under the conditions of Figure 4.2. The solid curve in both plots is the prediction for one-dimensional oscillation in the known effective potential, as sketched on the right. Quantitative agreement is seen here and in numerous data sets at different trapping parameters, as set forth in [19].

Trapped atoms in this system are tightly confined close to a single antinode of the field, with typical axial amplitude $\lesssim 50\,nm$ in simulations. Experimentally, detectable signatures from axial motion are not observed [25, 26, 19]; with our detection bandwidth of 100 kHz, the role of axial motion at $\sim$1 MHz would be to reduce the amplitude of the transmission signals we do observe, through an averaging effect. By analyzing the data for variation away from the radial predictions, we obtain an operational bound of $\lesssim 70\,nm$ for the amplitude of axial motion, in good agreement with simulations. This corresponds to a typical variation in $g_(\vec{r})$ due to axial motion of less than 7%.

Thus transmission provides a direct, real-time record of an atom's radial distance from the cavity axis; this record can also be used along with the known effective potential to reconstruct two-dimensional trajectories. An experimental trace of transmission vs. time for a single trapped atom is shown in Figure 4.4(a), with

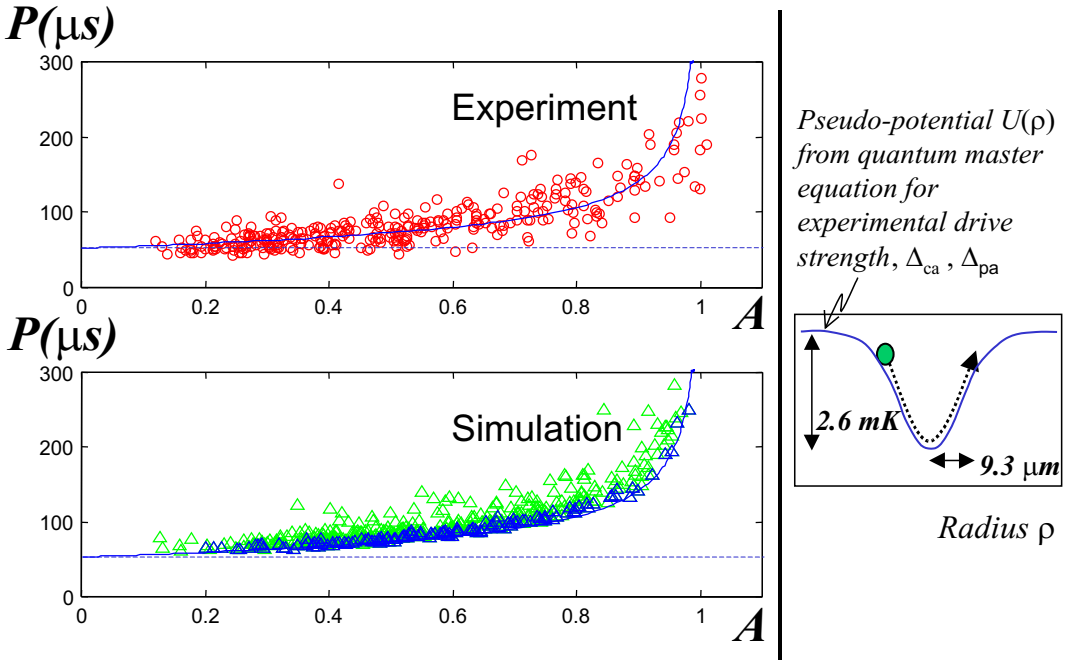

Figure 4.3: Period P vs. amplitude A of transmission oscillations for trapped atoms in experiment and simulation (parameters of Figure 4.2). Data agrees quantitatively with simulations and with the prediction from the known effective potential (solid line).

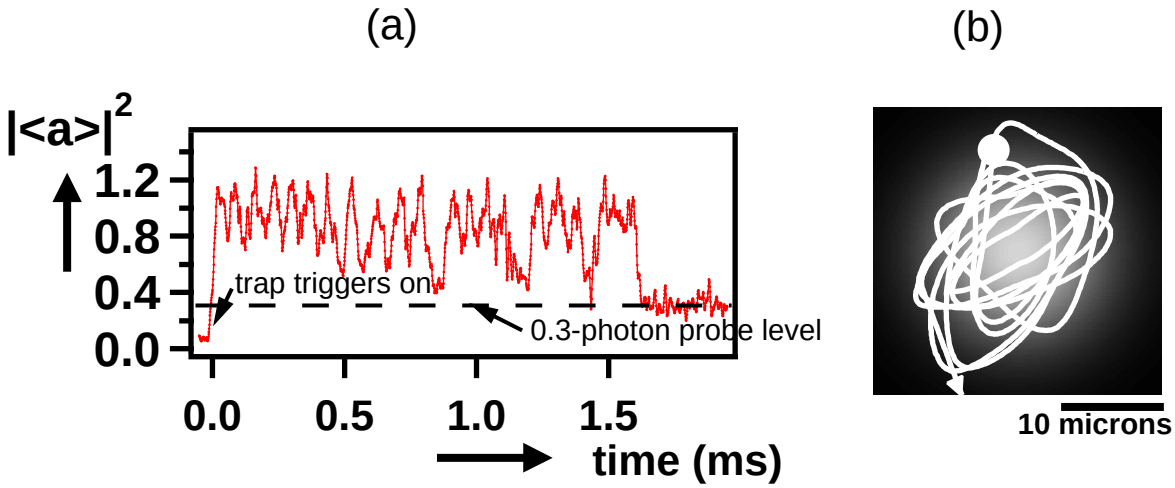

Figure 4.4: (a) Cavity transmission record for a trapped atom moving within the cavity mode (parameters of Figure 4.2). (b) Atomic trajectory in the radial (y,z) or (ρ, θ) plane as reconstructed from the transmission data of (a).

the corresponding reconstructed trajectory in Figure 4.4(b). The ball indicates an estimate in error of the reconstructed position, as discussed in the next section. Such reconstructions are tested by applying the method to simulated atomic trajectories. We note that while the two-dimensional reconstructions rest on the ability to neglect axial motion, it is in fact a "burst" of axial heating that typically ends an atom's dwell time in the cavity. This axial heating occurs rapidly, so that for the final half-cycle of atomic motion in the cavity our transmission signal *is* typically considerably affected by the average over axial motion, and the two-dimensional reconstruction is not reliable at its endpoints.

4.2 Reconstruction Algorithms and Validation

With axial motion neglected due to its small amplitude and the separation of timescales between it and radial motion, the cavity transmission $T(t)$ corresponds directly to a record of radial position $\rho(t)$. Because of the cavity mode's cylindrical symmetry, no information is directly provided about the angular position $\theta(t)$ of the atom in the transverse plane. However, since we know the radial effective potential via steady-

state solution to the quantum master equation, we can use the time record of $\rho(t)$ in this cylindrically symmetric potential to derive an estimate of the atom's angular momentum L and thus of $\dot{\theta}(t)$. In this way we are able to use the time record of the scalar quantity $T(t)$ to obtain a two-dimensional atom trajectory.

Because the motion is not completely conservative, but includes momentum diffusion and friction terms, angular momentum is not conserved and varies slowly during an atom's dwell time in the cavity. Thus we perform a running estimate of $L(t)$ rather than applying a single value L throughout a given trajectory. This variation of $L(t)$ and our ability to estimate it accurately provide important limits on the validity of such two-dimensional reconstructions, as discussed below.

The reconstruction algorithm is validated by applying it to transmission traces from simulated trapped-atom trajectories, with detection noise added. In simulations the reconstructed two-dimensional trajectory can be compared with the "actual" atomic position record to yield an estimate of error for the reconstruction method. The simulations themselves are presented in more detail in [26] and in Section 4.4.1 below. To ensure close correspondence with the detection noise in the experiment, actual "noise" data traces, taken at the appropriate transmitted powers, were added to the (otherwise noiseless) simulated transmission records.

The trajectory reconstruction algorithm is as follows (see Figure 4.5) :

- Transmission data is acquired at 100 kHz detection bandwidth and digitized at 1 megasample per second. The transmission record is then smoothed with a 20 kHz 5-pole Butterworth filter [81].

- We neglect axial motion as discussed above, assuming an atom to be confined to small-amplitude motion near a single antinode of the standing wave.

- From steady-state solution of the master equation, we know the cavity transmission as a function of atomic radius ρ. This relation is inverted through a lookup table (with linear interpolation) to turn our smoothed transmission trace into $\rho(t)$.

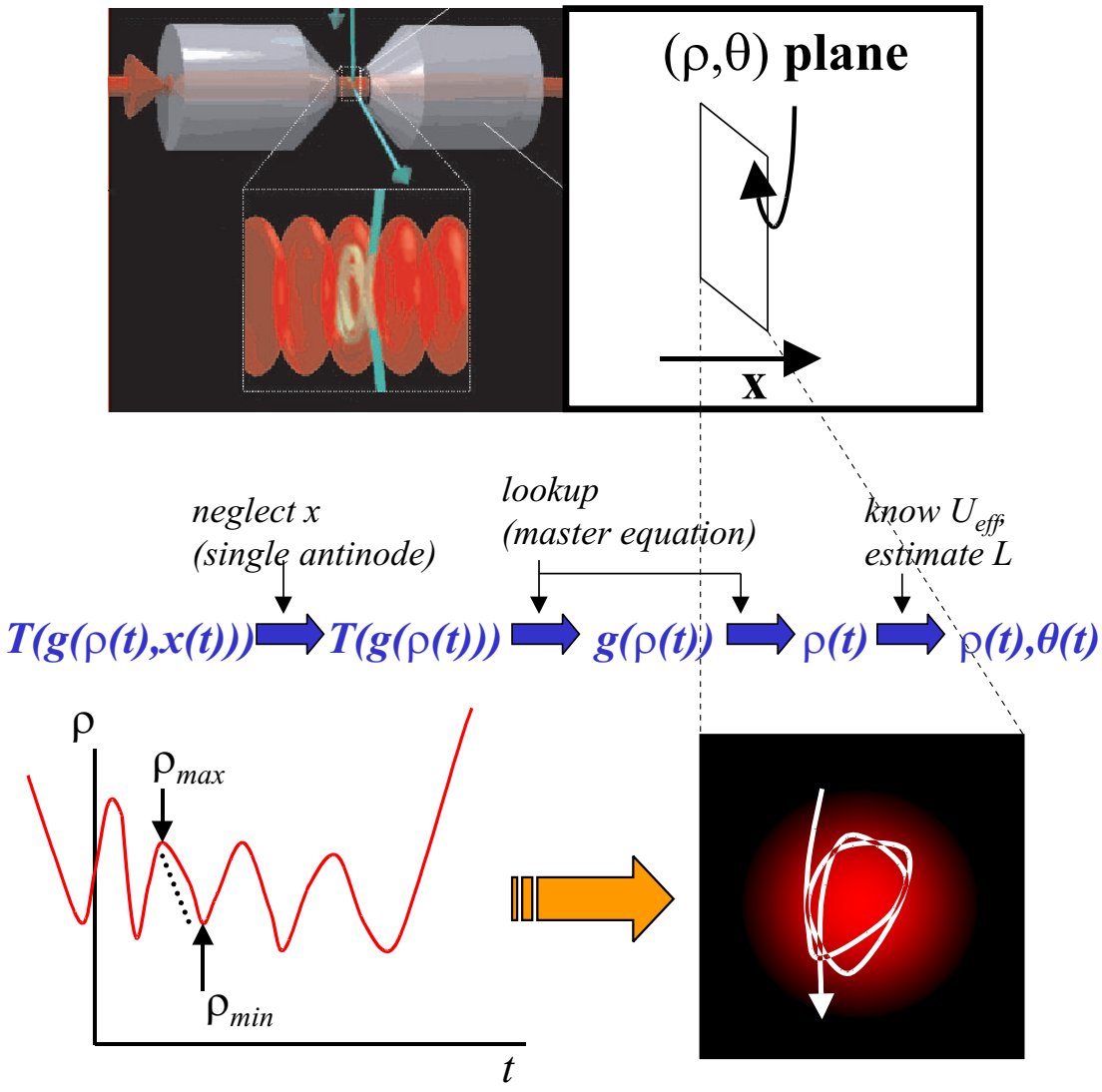

Figure 4.5: Principle of 2-D trajectory reconstructions

- Also from steady-state solution of the master equation, we know the potential $U_{eff}(\rho)$. We divide $\rho(t)$ into segments between a successive maximum and minimum radius, ρ^i_{max} and ρ^i_{min}. Now for each segment we calculate an angular momentum via

$$L_i = \rho^i_{max}\rho^i_{min}\sqrt{\frac{2m(U_{eff}(\rho^i_{max}) - U_{eff}(\rho^i_{min}))}{(\rho^i_{max})^2 - (\rho^i_{min})^2}}. \tag{4.1}$$

- Now we have a discrete set of stepwise angular momenta. We interpolate linearly between them for a "running" estimate $L(t)$.

- At each time now we have an angular velocity

$$\dot{\theta}(t) = \frac{L(t)}{m(\rho(t))^2} \tag{4.2}$$

- We start the trajectory at some angle θ_0 and use $\rho(t)$, $\dot{\theta}(t)$ to obtain a 2-d trajectory.

Three basic ambiguities will be clear from this algorithm, as illustrated in Figure 4.6: 1) the sign of the angular momentum is unknown, so the trajectory has arbitrary handedness. 2) the initial angle θ_0 is arbitrary, so the resulting trajectory can be rotated freely as a unit. Trajectories are presented with the atom entering from above in a physically plausible manner, since the atom is initially falling under the influence of gravity. 3) The trajectory is constructed in two dimensions, with the axial motion confined within a single antinode, but no information is available about *which* antinode the atom occupies during the trajectory.

Reconstructions of simulated trajectories are compared with the "actual" atomic position record by first adjusting the overall sign of the reconstructed angular momentum and the initial angle θ_0 for the best possible match. An estimate of error is calculated by comparing reconstructed and actual positions over a set of simulated trajectories, excluding in each trajectory the first and last half-cycles of radial motion. These initial and final cycles are not expected to reconstruct accurately due to lack of

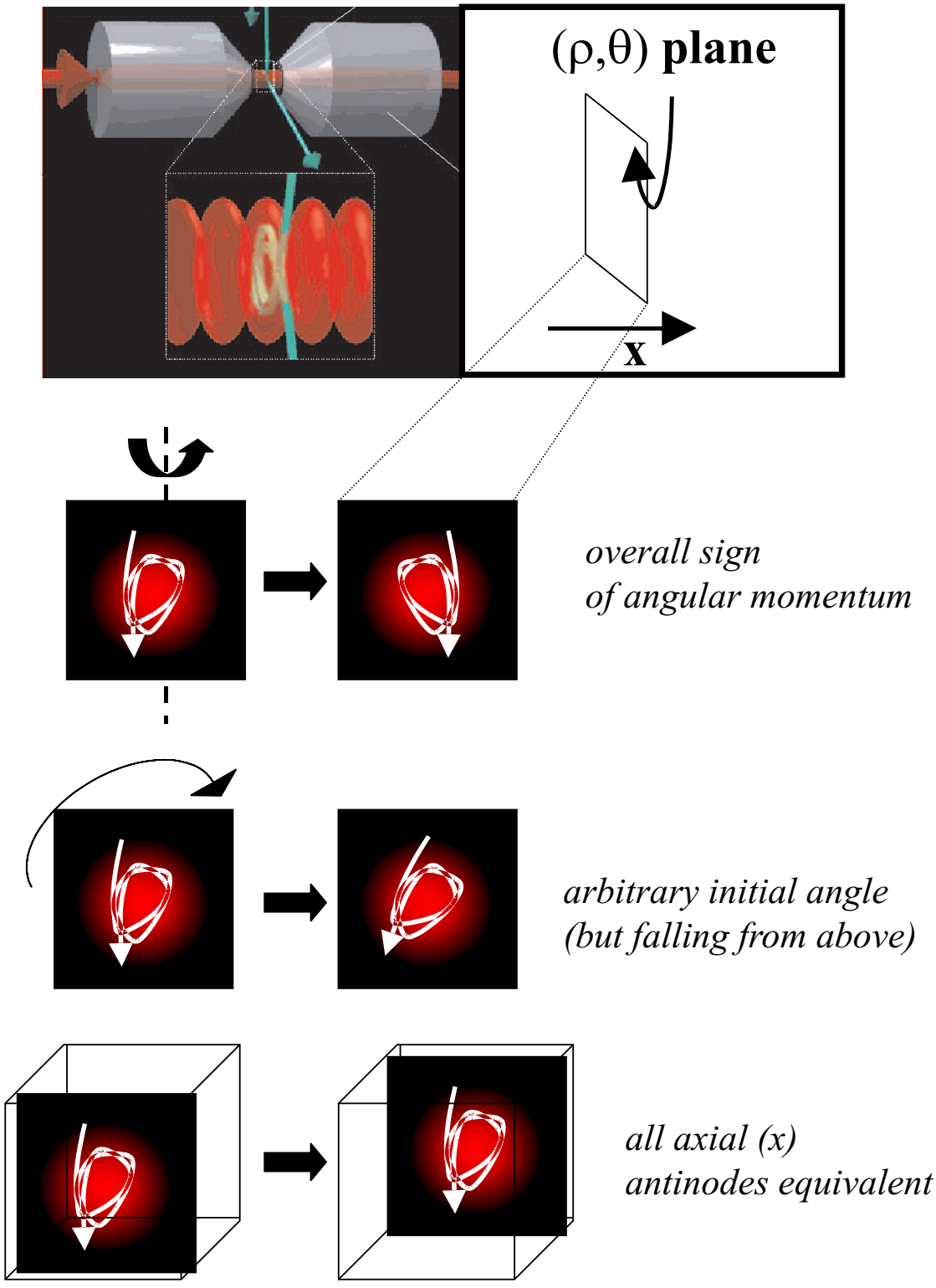

Figure 4.6: Basic ambiguities of reconstructed trajectories

confinement (for angular momentum estimation) and contamination from axial motion (as mentioned above). Several example reconstructions of simulated trajectories are shown in Figure 4.7.

Cases that cannot be reconstructed will also be clear from this algorithm and our preceding discussion. First, extremely linear trajectories cannot be reliably reconstructed because their angular momentum is so small that momentum diffusion can change them by up to (and above!) 100% during a fraction of a radial oscillation cycle. Reconstruction of such trajectories (that pass extremely close to the origin and significantly far away again) should not be attempted. These cases (about one quarter of trajectories in simulated and experimental data sets) are recognized with an estimated 97% success rate via cavity transmission traces where the transmission consistently reaches the maximum "allowed" value. Indeed the algorithm fails or gives nonsensical trajectories if these cases are attempted, as shown in Figure 4.8.

Second, trajectories that closely approach the origin (within a micron or so) cannot be reliably reconstructed from this algorithm and the data we use. The issue here is that at our probe detuning (near the lower Rabi sideband), $g(\rho)$ and thus also $T(\rho)$ are nearly flat near $\rho = 0$. In principle this problem can be overcome with improved detection schemes; I return to this question briefly at the end of Section 4.3. We note that while this limitation may seem similar to the first one, and indeed both apply to many of the same experimental data traces, they are rather fundamentally different. One is a limit arising from dynamical noise (compared to motional timescales), while the second is an issue of detection sensitivity.

Finally, the algorithm as stated above cannot deal with the case of a perfectly circular orbit which yields an angular momentum estimate of zero over zero. One might think that nearly circular orbits would be hopelessly mangled by this algorithm, especially as noise obscures what small radial variations there are. In fact, nearly-circular orbits work quite well, since the algorithm finds small wiggles (either real or noise-related) and uses them to calculate an angular momentum which is nearly that of the circular orbit at that radius. The resulting trajectory reconstruction is in fact very good, as illustrated by the examples in Figure 4.9.

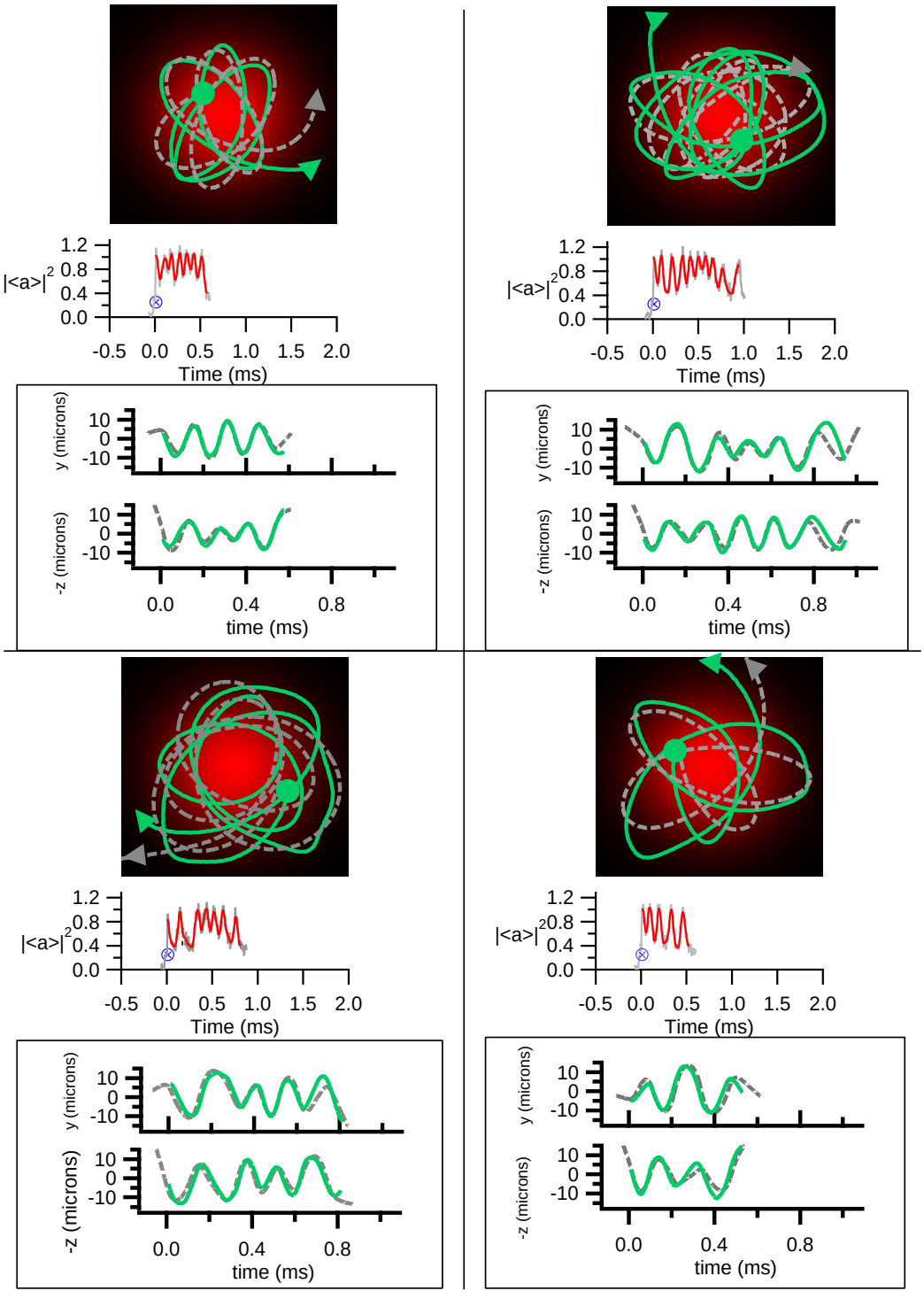

Figure 4.7: Example trajectory reconstructions from simulated transits (parameters of Figure 4.2). The two-dimensional trajectory is shown on a square 30 μm on a side. Dotted lines indicate the "actual" simulated trajectory while solid lines show the reconstruction. In transmission traces, the filtered transmission is shown as a dark trace overlaid on the original noisy transmission signal.

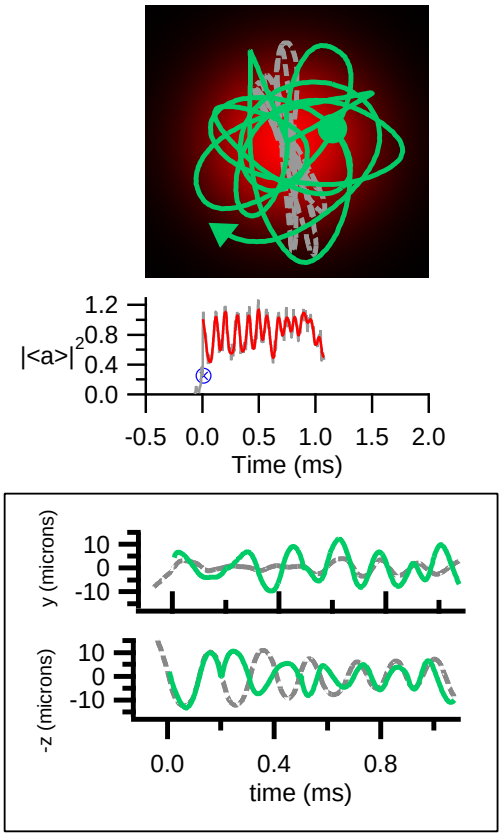

Figure 4.8: Example failed trajectory reconstruction for a linear trajectory (parameters of Figure 4.2). The two-dimensional trajectory is shown on a square 30 μm on a side. Dotted lines indicate the "actual" simulated trajectory while solid lines show the reconstruction. In transmission traces, the filtered transmission is shown as a dark trace overlaid on the original noisy transmission signal.

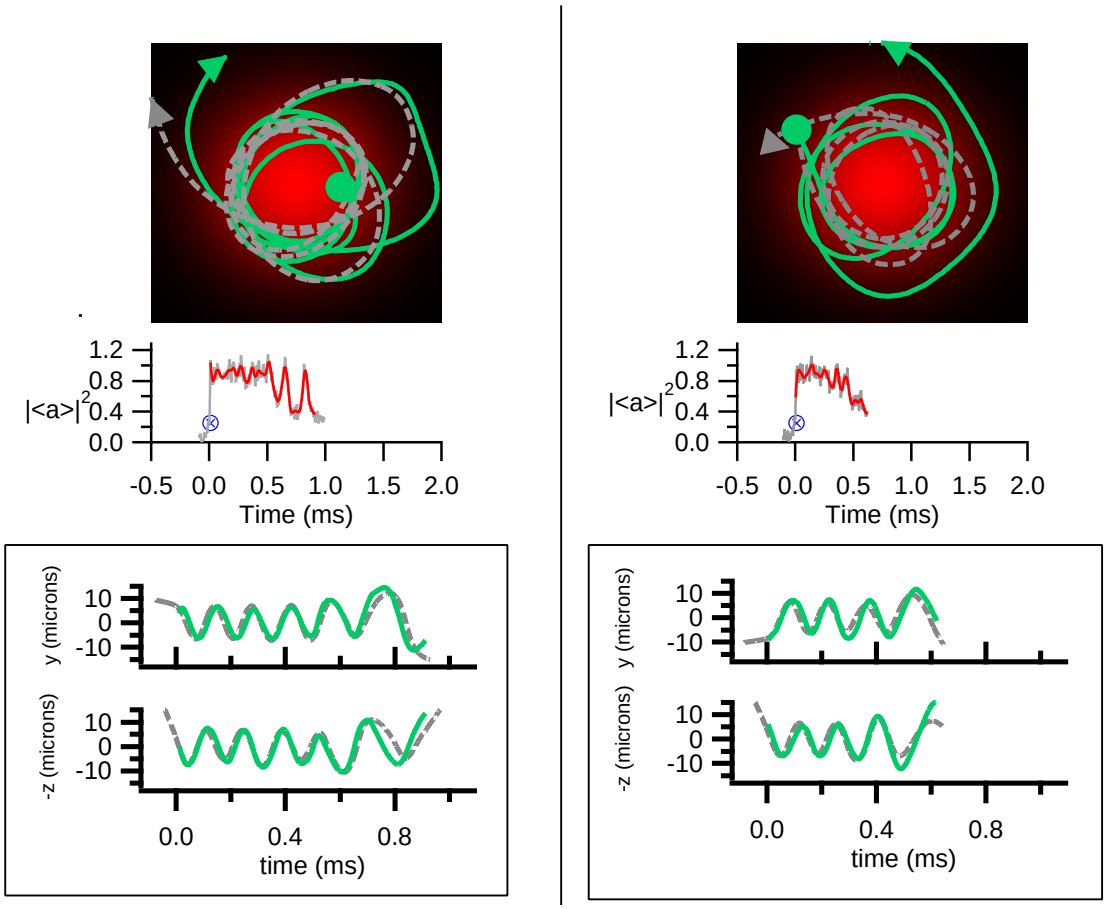

Figure 4.9: Example reconstructions of nearly circular trajectories (parameters of Figure 4.2). The two-dimensional trajectory is shown on a square 30 μm on a side. Dotted lines indicate the "actual" simulated trajectory while solid lines show the reconstruction. In transmission traces, the filtered transmission is shown as a dark trace overlaid on the original noisy transmission signal.

A possible stumbling-block for our trajectory reconstruction method is the case of the trapped atom which has small-amplitude axial motion, heats out of the antinode in a rapid "burst" as described above, but then *falls back into an antinode* due to the action of friction and/or momentum diffusion. Such an event (an atom "skipping" between antinodes) would have cavity transmission contaminated by a brief episode of large-amplitude axial motion in the middle of the trajectory, causing our algorithm to estimate $\rho(t)$ wrongly during the "skipping." In a survey of a simulated data set of 410 trapped-atom trajectories of more than one radial oscillation cycle, fifteen exhibited "skipping," giving an $\approx 4\%$ rate for this particular issue. I mention this rate here because it is rather different from (considerably smaller than) the likelihood for axial "skipping" in some other parameter regimes, as discussed more fully in [26].

4.2.1 Note on Conservative Motion in Gaussian Potentials

As a point of reference when viewing these atomic trajectories, it is interesting to note some characteristics of perfectly conservative two-dimensional motion in the same effective potential. The potential, while not strictly analytic in form, is very closely fit by a Gaussian in ρ. Conservative motion in this cylindrically symmetric potential produces trajectories which are in general not closed. Closed trajectories do arise – trivially, for zero angular momentum or circular orbits, or for small-energy motion that samples only the harmonic portion of the potential.

4.3 Position Sensitivity Estimates

The trajectory reconstructions described above, with their validation and error estimates from comparison with simulations, correspond to an atomic position measurement with 2 μm resolution achieved in a timescale of 10 μs. This corresponds to a position sensitivity of $\sim 20\, nm/\sqrt{Hz}$ [25, 19].

We may compare this with a quick estimate of sensitivity limits for our cavity and detection scheme (Figure 4.10). We begin by writing down a rough dependence of measured cavity transmission on the atomic radial position: d(detected photons per

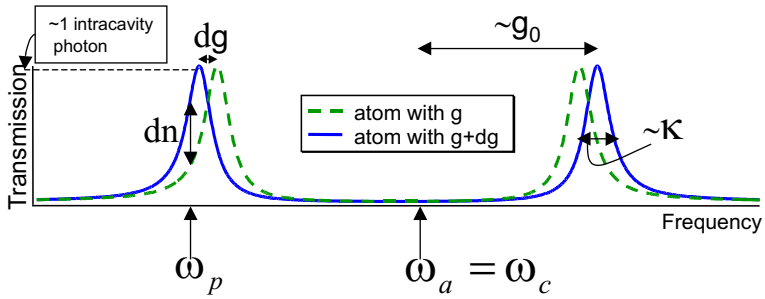

Figure 4.10: Sketch of vacuum Rabi splitting as the basis for position sensitivity estimates.

time)/dρ = $\eta 2\kappa \frac{dn}{dg}\frac{dg}{d\rho} = 2\eta\kappa\frac{1}{\kappa}\frac{g_0}{w_0} = 2\eta\frac{g_0}{w_0}$ (η is the overall detection efficiency and 2κ is the overall cavity decay). Here we have approximated $\frac{dn}{dg} \sim \frac{1}{\kappa}$ by reasoning that the intracavity photon number drops from ~ 1 to ~ 0 over the resonance feature width of $\sim \kappa$. Our result then implies that, as an atom moves over distance $\Delta\rho$, the corresponding signal (change in detected transmission) is $2\eta\frac{g_0}{w_0}\Delta\rho$.

To turn this into a sensitivity, we must ask how finely we can resolve a change in the number of detected photons per unit time. That is a question of how big the noise is relative to the signal. Overall there is roughly one photon in the cavity, giving a photon-detection rate of $\eta(2\kappa)$. Thus the shot noise is proportional to that value, i.e., shot noise for a given detection bandwidth B is $\sqrt{2\eta\kappa B}$. The signal-to-noise ratio in a given bandwidth B is $\sim 2\eta\frac{g_0}{w_0}(\Delta\rho)/\sqrt{2\eta\kappa B}$. Now if we define the sensitivity S_ρ as the $\Delta\rho$ detectable with unit signal-to-noise, we have $S_\rho \sim \sqrt{\frac{1}{2\eta}}\frac{w_0}{\sqrt{g_0^2/\kappa}}\sqrt{B}$. Substituting the relevant experimental values, this analysis yields a position sensitivity limit of $\sim 1.0\, nm/\sqrt{Hz}$. The discrepancy between this quantity and the measured sensitivity can be somewhat attributed to technical noise – since technical noise is comparable to the shot noise it should degrade the signal-to-noise and thus the sensitivity by a factor of $\sqrt{2}$ or so. That still leaves a very large gap, partially to do with the crude estimates of the physics going on. The fact of the matter is that there is excellent sensitivity on the side of the cavity mode ($\rho \sim w_0/2$) and rather poor sensitivity on-axis ($\rho \ll w_0$) and at the edges($\rho \gg w_0$), while we average over everything. Furthermore, our detection method falls short of realizing a full g_0^2/κ information rate for sensing an atom in the cavity, as discussed more fully in Chapter 7.

To predict a sensitivity for the as-yet unobserved axial motion, we may replace w_0 with $\lambda/4$, the axial distance from field node to antinode, in the estimates above. This yields a limit of $0.015\,nm/\sqrt{Hz}$ in principle, or an extrapolated sensitivity of $0.3\,nm/\sqrt{Hz}$ based on what we achieve in the transverse direction. However, the increased sensitivity in the axial direction is offset somewhat in usefulness by the correspondingly faster timescale for axial motion, meaning that to resolve the motion on relevant dynamical timescales a higher measurement bandwidth must be employed.

From the point of view of quantum measurement and feedback schemes, it is of considerable interest to compare our position sensitivity with the limits imposed by the Heisenberg uncertainty principle – or, for quasi-continuous weak measurements such as ours, the standard quantum limit. Following the analysis of [82] for broadband position observation on a free particle, we estimate the time t_* for backaction effects to become discernible in the measurement record. Taking our radial sensitivity of $2\,\mu$m over 10μs, the walk-off time is $t_* \approx 1.5\,ms$. This means we could just begin to see the effect in the longest transits, while the mean dwell time puts us about a factor of five from the standard quantum limit.

One caveat in this analysis is the application of the free-particle theory to this case in which the atom is in fact trapped; certainly another important consideration in discussing the quantum nature of the atomic motion will be the vibrational quantization of atomic motion in the trap. In the current experiments, quantization is irrelevant in the radial dimension, where the vibrational frequency is 9.4 kHz compared to typical energies of 9.8 MHz. However, in the tightly-bound axial direction the vibrational levels are spaced by 0.7 MHz, which begins to be comparable to the typical axial energy of about 3 MHz during most of a trapped atom's lifetime.

Improved signal-to-noise is undoubtedly desirable for developing "atom-cavity microscopy" and exploring quantum measurement limits. One opportunity for improved sensing would be to incorporate full detection of the cavity output field, i.e., amplitude and phase of $\langle a \rangle$ rather than the $|\langle a \rangle|^2$ measurement we now peform. Such full detection has been implemented in a cavity QED setting in [47], where atom-transit "phasors" were observed. In that work the ability to access phase-shift information

for the cavity field opened up the possibility for high signal-to-noise observations in a farther-detuned regime. Besides that possibility, full detection in our scenario would enhance signal-to-noise for observations of atoms passing very close to optimal coupling, with $g(\vec{r}) \approx g_0$.

4.4 Why Do Reconstructions Work in *This* Parameter Regime?

In this section we examine more closely the trapping potential and momentum diffusion of the triggered-trapping experiment. This analysis, largely presented in [26], was originally motivated by a desire to understand two aspects of our experiment. First, to what extent was it important that the trapping was a "binding" between a single atom and a single photon rather than an optical dipole force trap for a single atom with a classical light field? Second, how could we characterize the dynamics that made the motion of our trapped atoms quasi-conservative (and thus allowed trajectory reconstructions), especially considering the very different trapped-atom dynamics in a conceptually similar experiment (Pinkse *et al.*, [50])? I present this material here largely because it helps to characterize the dynamical regime that allows trajectory reconstructions, thus filling out the discussion of Section 4.2. Furthermore, the qualitative nature of the dynamics as reflected in the potentials and heating rates provides a relatively simple way of predicting conservative vs. diffusive trap dynamics in other parameter regimes; this is a useful tool in evaluating dynamics for different optical cavities, as discussed here and in Chapter 7.

To begin with we elucidate the quantum vs. classical nature of the trapping potential and momentum diffusion. In particular we find that, for the parameters of the atom-cavity microscope [25], the trapping potential and momentum diffusion have a quite different character from what would be expected of an equally deep standing-wave trap in free space. The usual (semiclassical) fluctuations of the dipole force along the standing wave are suppressed by an order of magnitude, which represents quali-

tatively new physics for optical forces at the single-photon level within the context of cavity QED. In the parameter regime of Pinkse *et al.* [50], still in the strong-coupling limit but with larger critical parameters (m_0, N_0), the situation is rather different. The cavity and atom in this experiment had $(g_0, \kappa, \gamma_\perp)/2\pi = (16, 1.4, 3)$ MHz. For these parameters, even when the atom-cavity system is strongly coupled and driven such that it has a mean intracavity photon number of roughly one, the trapping potential and momentum diffusion are only slightly different from those in a free-space standing wave. We show that in the parameter regime of [50] the heating rates are such that the atom could be expected to gain energy equal to a significant fraction of the total trapping potential during a single motional oscillation period for both axial and radial motion. By this measure the heating rates in the atom-cavity microscope are very much slower, indicating more nearly conservative motion, and this could be expected to have a profound effect on the qualitative nature of the dynamics in the two experiments.

Ref. [26] also presents simulated transits for both experiments, and discusses the qualitative features of atomic dynamics in both cases. For the parameter regime of the atom-cavity microscope, conservative radial motion dominates diffusion and standing-wave motion, with atomic trajectories localized at peaks of a single standing-wave antinode. Atoms trapped with the mean trapping time execute several radial orbits. The eventual escape is typically due to heating along the cavity axis. By contrast, for the experiment of [50], a trajectory of typical duration does not experience a complete radial orbit and in fact resembles a scattering event, with a large contribution from radial diffusion as well. For these events the observed localization time is comparable to the time for free flight through the cavity. Axially the simulations show that in longer-duration transits the atom frequently skips between wells of the standing-wave potential due to repeated heating and recooling.

4.4.1 Quasi-classical Model for Atomic Motion in the Cavity

The atom-cavity system is modeled by a quasi-classical treatment presented in [26, 83]; the term *quasi-classical* is used to distinguish this approximation from the usual *semiclassical* treatment which neglects the full quantum nature of the cavity field. Here, the atomic internal states and cavity field are treated with their full quantum character retained. The atomic motion is treated in a quasi-classical approximation which requires the spread of its wavepacket in both position and momentum space to be small compared to relevant scales in the problem. Specifically, an atom must be localized to much better than an optical wavelength of the atom or cavity resonance frequencies. This is equivalent to the requirement that the momentum spread be large compared to an individual momentum kick associated with spontaneous emission or exchange of excitation with the cavity field. At the same time, however, an upper bound on momentum spread (or equivalently lower bound on position spread) must be satisfied. This bound arises by considering the Doppler shifts of relevant fields as seen by the atom; Doppler shifts due to the momentum spread must be small relative to atom and cavity linewidths. The consistency of these conditions and their application to the atom-cavity system rely on a separation of timescales between atomic motion and atom-cavity internal dynamics; this separation is easily satisfied for motion in the radial direction, and still applicable though approaching its limit for motion in the axial dimension. Under these conditions we may calculate all quantities of interest in the system by referring to steady-state solutions of the master equation (Equations 2.6-2.7) for each atomic position $\vec{r}$.

The treatment outlined above and fully set forth in [26, 83] can give us a great deal of information about the nature of the dynamics that may be expected in the parameter regimes relevant to the atom-cavity microscope and to [50]. In particular we are interested in whether quantization of the cavity field leads to any significant change in the dynamics, in the sense of asking whether the atomic motion is very different in the cavity from what it would be in a free-space standing wave of the same intensity and geometry as the cavity mode. Secondly, we can investigate the nature

of the resulting atomic motion in the cavity field, which can be either predominantly conservative or significantly diffusive and dissipative, depending on the particular parameters of interest.

To get a feel for the type of atom dynamics expected, effective potentials and heating rates were calculated for both the axial and the radial directions of motion. Friction coefficients may also be calculated, but we omit them in this discussion because their contribution to the motion is much smaller than that of momentum diffusion in the atom-cavity microscope. The force operator is given by

$$\hat{\vec{F}}(\vec{r}) = -\hbar\vec{\nabla}g(\vec{r})(\hat{a}^\dagger\hat{\sigma} + \hat{a}\hat{\sigma}^\dagger) = -\hbar g_0\vec{\nabla}\psi(\vec{r})(\hat{a}^\dagger\hat{\sigma} + \hat{a}\hat{\sigma}^\dagger). \tag{4.3}$$

The effective potential for the atom in the cavity field may be calculated from the force by

$$U_{eff}(\vec{r}) = -\int_0^{\vec{r}} \langle\hat{\vec{F}}(\vec{r}')\rangle \cdot d\vec{r}'. \tag{4.4}$$

The heating rates represent the average increase in the motional energy due to the momentum diffusion at a given position $\vec{r}$ and may be calculated from the diffusion tensor according to

$$\frac{dE}{dt}(\vec{r}) = \mathrm{Tr}[\mathbf{D}(\vec{r})]/m, \tag{4.5}$$

where m is the atomic mass. The total momentum diffusion tensor $\mathbf{D}$ has two distinct contributions D and E. The first contribution arises intuitively from decays and re-excitations which switch the system stochastically between the trapping potential of the strong-field seeking state and the flat potential of the overall ground state. This contribution to momentum diffusion is given by

$$D_{ij} = \int_0^\infty d\tau[\frac{1}{2}\langle\hat{F}_i(\tau)\hat{F}_j(0) + \hat{F}_i(0)\hat{F}_j(\tau)\rangle - \langle\hat{F}_i\rangle\langle\hat{F}_j\rangle]. \tag{4.6}$$

(Recall that the time dependence of $\hat{F}$ arises because we are in the interaction picture with respect to the probe frequency ω_p.) The other contribution to momentum diffusion comes simply from momentum kicks associated with atomic spontaneous

emission, and is given by

$$E_{ij} = \varepsilon_{ij}\hbar^2(2\pi/\lambda)^2\gamma_\perp\langle\hat{\sigma}^\dagger\hat{\sigma}\rangle. \tag{4.7}$$

Here ε describes the usual dipole distribution of atomic spontaneous emission and is diagonal, with $\varepsilon_{xx} = \frac{2}{5}$ and $\varepsilon_{yy} = \varepsilon_{zz} = \frac{3}{10}$.

Since $g(\vec{r}) = g(\rho, x)$, we neglect the θ coordinate for the time being and write the potentials and diffusions as functions of position (ρ, x).

4.4.2 Potentials and Heating Rates for Atomic Motion

Gathering up the results – and notation – of the preceding discussion, we see for example that the axial potential at the center of the Gaussian mode is $U_{eff}(0,x) = -\int_0^x \langle\hat{\vec{F}}(0,x')\rangle dx'$ and the associated axial heating rate is $dE(0,x)/dt = \mathbf{D_{xx}}(0,x)/m$. These quantities along with their radial equivalents $U_{eff}(\rho,0)$ and $dE(\rho,0)/dt$ are plotted in the solid traces of Figure 4.11 for the parameters of the atom-cavity microscope. The force and momentum diffusion coefficient for the cavity system were calculated according to the formulae described above by numerical techniques based on [34, 83]. The field state is expanded in terms of number states and truncated at an appropriate level and a matrix continued fraction algorithm is used to calculate D. The axial potentials and heating rates have $\lambda/2 = 426$ nm periodicity inherited from the standing-wave field strength. Observe that the axial heating rates have minima at both field antinodes and field nodes.

The first thing to note is that the axial and radial heating rates are very different from one another. In the radial direction, heating is dominated by diffusion due to spontaneous-emission recoils. Axially, however, the reactive or dipole fluctuation component of the diffusion dominates. This is because the reactive component is proportional to the gradient of the field squared, which is much larger for the axial direction where variations are greater (by a factor of $2\pi w_0/\lambda$). This contribution also has the property that it does not saturate with the atomic response.

It is already clear that it should be possible to trap individual atoms, since the

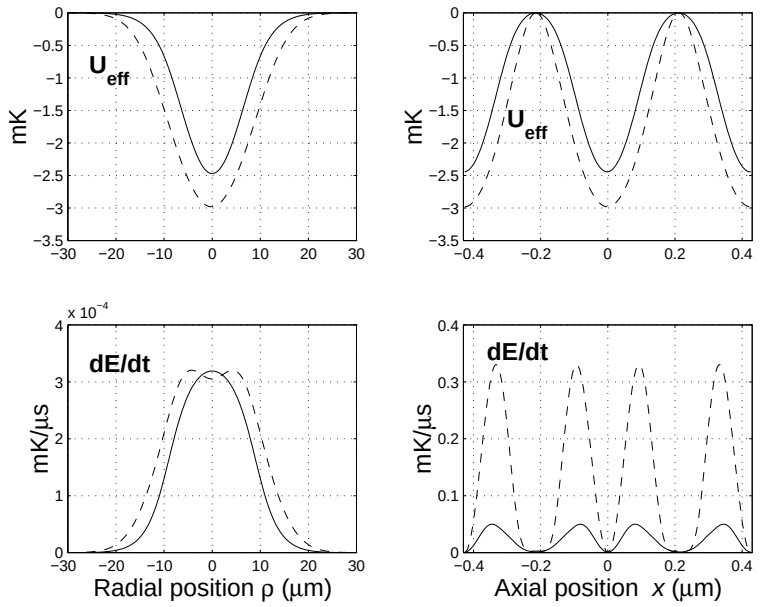

Figure 4.11: Effective potentials and heating rates for the ACM parameters, with $(g_0, \kappa, \gamma_\perp)/2\pi = (110, 14.2, 2.6)$ MHz. Detunings are $(\Delta_{pa}, \Delta_{ca})/2\pi = (-125, -47)$ MHz and the drive strength corresponds to 0.3 photons in the empty cavity. The quantum prediction is shown by solid lines, with the semiclassical prediction given in dashed lines.

potential depth of roughly 2.5 mK is greater than the initial energy of the atoms in the experiment (around 0.46 mK) and the heating rate in the radial potential is relatively slow. Over 50 μs (a timescale over which the atomic motion is strongly affected by the potential) the total heating will typically still be small compared to the depth of the potential. However, the importance of the quantum character of the relevant fields or phenomena is not ensured by the statement that trapping occurs with mean field strength of about one photon, since this is trivially the case in an equivalent free-space volume for a field of the same intensity as that inside the cavity. Just as in the cavity, a free-space field at $\omega_p < \omega_a$ creates an attractive potential which leads to the well-known red-detuned dipole trap for neutral atoms (see, e.g., [32]); whether the intracavity trap differs in any recognizable way from its simple free-space cousin is not immediately clear.

In order to see whether a full quantum description of the atom-cavity is necessary in order explain observed effects, Figure 4.11 also shows the values calculated for an

atom in an equivalent free-space standing wave, calculated by standard techniques [84]. This free-space standing wave has the same geometry as the cavity mode and the same peak field strength $g_0|\langle a\rangle|^2(0,0)$. The detuning between the free-space field and the atom is chosen to be Δ_{pa}. Perhaps surprisingly, the only large difference between the two models is in the axial heating rate, where a strong suppression of the axial heating is seen in the quantum calculation. This suppression is an effect of the quantized nature of the intracavity field. The self-consistent coupling of the cavity field and atomic position (in a semiclassical sense) cannot explain this suppression; in fact, by itself this coupling would lead to an increase in diffusion over the free-space case, since the atomic motion within the cavity induces steeper gradients in the field. The suppression of diffusion is then evidence that it is necessary to use a fully quantum description, and speak of single photons rather than classical fields for these experimental parameters. As discussed in [25], this suppression of the axial heating was essential for the trapping of atoms in the cavity. Thus for these experimental parameters, the eigenvalue structure of Figure 2.5 leads to profound differences between the standard theory of laser cooling and trapping and the extension of this theory to the regime of strong coupling in cavity QED.

By way of comparison, the same quantities are plotted for the parameters relevant to Pinkse *et al.* [50] in Figure 4.12. The smaller value of g_0 in this experiment leads to a smaller effective potential, since the spatial gradients of the dressed state energy levels (which lead to the potential) are proportional to g_0. More importantly, the diffusion values calculated from the full quantum model discussed above are now little different from those of the equivalent free-space standing wave. This lack of a clear difference in potentials or diffusion indicates that the quantized nature of the field is not required to explain the radial trapping observed in [50]. Note that the resulting axial heating rates are essentially the same as those of Figure 4.11 in absolute magnitude; however, in the atom-cavity microscope the potential has been made deeper *without* the expected corresponding increase in diffusion. For the parameters of [50] one additional interesting feature appears – enhanced cooling of the atomic motion relative to the parameters of the atom-cavity microscope. This

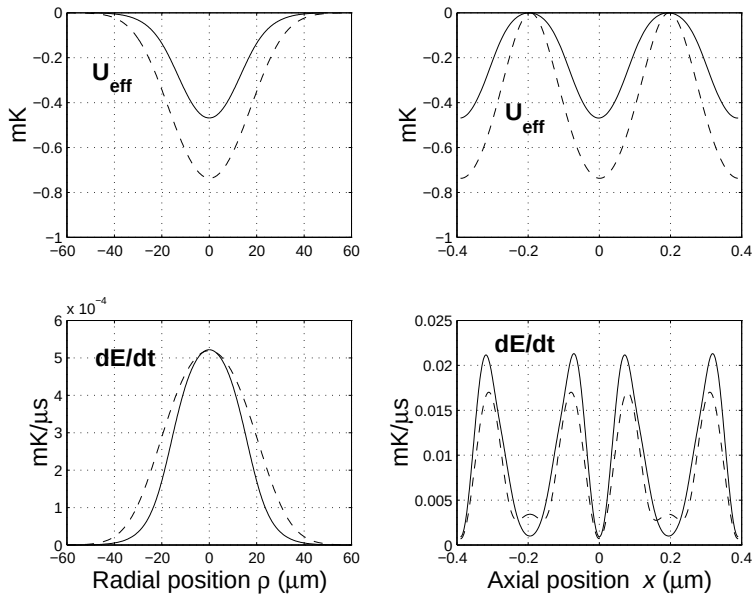

Figure 4.12: Effective potentials and heating rates in a less conservative parameter regime. Here $(g_0, \kappa, \gamma_\perp)/2\pi = (16, 1.4, 3)$ MHz. Detunings are $(\Delta_{pa}, \Delta_{ca})/2\pi = (-40, -35)$ MHz, and the drive strength corresponds to 0.9 photons in the empty cavity. Solid lines are the quantum prediction while dashed lines are the result of the semiclassical calculation. Note that axial quantities here have a periodicity of 390 nm, since this experiment used Rubidium atoms with a resonant transition at 780 nm.

arises through cavity-mediated cooling [85, 86], and has an important effect on the axial dynamics of atoms in the experiment of [50].

We now wish to use these potentials and heating rates to gain an intuitive understanding of the character of atomic motion that we would expect to observe in each case. In particular, we are interested in exploring the degree to which the atomic motion in the potential can be close to conservative motion, or likewise the degree to which it could be dominated by diffusion.

The timescales of relevance to the conservative motion may be characterized by the period associated with small-amplitude oscillations in the bottom of the axial ($\tau_a = 1/\nu_a$) and radial ($\tau_r = 1/\nu_r$) potential wells. If the energy changes only by a small fraction of the total well depth U_0 over this timescale, motion will be nearly conservative. Figure 4.13 plots the potentials and heating rates for the two cases in this new set of scaled units; heating rates are expressed as an energy increase per

oscillation period, as a fraction of U_0 (note as the atom heats and explores the anharmonicity of the potential, the period of oscillation only lengthens). Interestingly, we see a clear qualitative difference in the nature of the atomic motional dynamics. For the parameters of the atom-cavity microscope (solid lines), in the radial plane spontaneous emission gives only small perturbations to the energy over the timescale of single orbits, and motion is nearly conservative. We note that this low level of diffusion enabled the reconstructions of single atom trajectories presented earlier in this chapter, for which the small changes in angular momentum could be accurately tracked. A quite different regime is found for the parameters of [50] (dash-dotted lines), where the radial atomic motion is strongly affected by heating from spontaneous emission kicks. Here an average atom gains an energy of nearly half the well depth in what would be a radial orbit time, adding a large diffusive component to the motion. This same scaling shows that the axial heating rate is also much more rapid on the scale of the potential in [50], which suggests that the atom will more quickly escape its confinement near an antinode and begin to skip along the standing wave. The qualitative understanding of the atomic motion gained here is borne out by the results of [25] and [50], and is explored in more detail in the simulations of [26].

From comparison of Figure 4.13 with simulated dynamics in [26], we arrive at a means for predicting the conservative or diffusive nature of single-photon trapping for atoms in varying parameter regimes. For example, I have calculated effective potentials and diffusion rates for a hypothetical triggered-trapping experiment in the cavity currently used in the other cavity QED lab in our group. This cavity has $(g_0, \kappa)/2\pi = (32, 4)$ MHz and a mode waist of $w_0 = 23.8\,\mu$m. The corresponding critical atom and photon numbers are $(N_0, m_0) = (2.0 \cdot 10^{-2}, 3.3 \cdot 10^{-2})$. For comparison, the atom-cavity microscope parameters were $(g_0, \kappa)/2\pi = (110, 14.2)$ MHz, giving $(N_0, m_0) = (6.1 \cdot 10^{-3}, 2.8 \cdot 10^{-4})$, with a mode waist of $w_0 = 14.1\,\mu$m.

I approximated the atom-cavity microscope conditions by keeping the cavity-atom detuning Δ_{ca} constant relative to g_0 and placing the probe a fixed fraction of κ inside (to the blue of) the lower dressed state resonance. Thus for the longer cavity (and smaller g_0, κ) I set $(\Delta_{pa}, \Delta_{ca})/2\pi = (-37, -14)$ MHz. To consider a single-photon

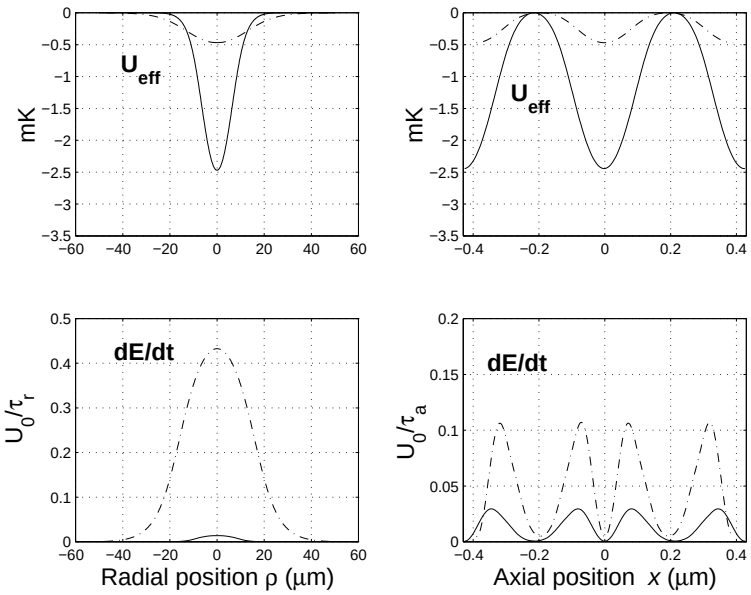

Figure 4.13: Heating per motional cycle measures conservative character of motion. Solid lines show the parameters of the atom-cavity microscope, while dash-dotted lines correspond to the situation of [50].

trapping experiment, I set a driving level of 0.3 photons in the empty cavity at this detuning. For this case I found an effective potential depth of $U_0 = 0.57\,mK$, with radial momentum diffusion giving a heating rate $dE/dt = 0.21U_0/\tau_r$. Axial motion was also characterized by higher momentum diffusion per motional cycle than we experienced in the atom-cavity microscope. Thus a single-atom, single-photon trapping experiment in this cavity would, not surprisingly, yield dynamics similar to those of [50] rather than to those of the atom-cavity microscope. Decreasing critical atom and photon numbers induces a transition from atom-cavity scattering experiments to largely conservative atom-cavity binding; in this sense the atom-cavity microscope could as well be termed the atom-cavity molecule.